Neural Oscillations in the Primary Visual Cortex of Mice

Mohammad Keshtkar

Supervisors:

Romain Ligneul

Mathilde Bonnefond

Research Lab:

Centre de Recherche en Neurosciences de Lyon (CRNL)

Acknowledgements

Table of contents

1 Introduction

1.1 Background

How does the brain efficiently process the overwhelming amount of sensory input that it receives from a constantly changing and uncertain environment? According to the predictive coding (PC) framework, the brain's key solution is to actively predict incoming sensory input based on past observations and to prioritize the processing of unpredicted sensory information (Huang and Rao 2011). PC envisions the brain as a prediction machine, where predictions are made through prior experience or expectation. These predictions are compared to the actual sensory input, and the difference, known as prediction error, is used to refine the internal model of the environment and orient attention towards unexpected features of the input. This allows the brain to minimize the prediction error and allocate its finite resources more efficiently (Vinck, Uran, and Canales-Johnson 2022).

Predictive coding is generally thought to be implemented by the cortex. Indeed, the mammalian cortex is organized hierarchically, with lower level areas processing more basic sensory features and higher areas integrating this information into more complex representations (Felleman and Van Essen 1991). Visual cortex is a prime example of this hierarchy, with primary visual cortex (V1) processing simple visual features like contrast and edges and higher visual areas (e.g. V2, V4) extracting more complex features of stimuli like texture and shape (Huff, Mahabadi, and Tadi 2018). The hierarchy of cortical processing allows the brain to make predictions at multiple levels of abstraction and compare these predictions to the actual sensory input. According to PC, communication between hierarchical cortical areas occurs through feedforward (FF) and feedback (FB) connections. FB projections involve top-down propagation of prediction from higher to lower-level areas, while FF projections involve bottom-up assembly of sensory input and prediction error from lower to higher-level areas to update the internal model. FF and FB connections have distinct laminar origins and targets within the cortex. FF connections mainly originate from layers 3 and 5 (of lower areas) and target the layer 4 (of higher area). On the other hand, FB connections arise from layers 2 and 6 (of higher areas) and target all layers except for layer 4 (of lower areas) (Vinck, Uran, and Canales-Johnson 2022).

Prominent studies in primates visual systems (Van Kerkoerle et al. 2014) suggest neural oscillations might play an important role in communication between cortical regions through FF-FB connections. The studies found that FF propagation is associated with gamma-band oscillations (30–100 Hz), while FB propagation involves alpha-band oscillations (8–12 Hz). Similarly, a study on mice vision

(Aggarwal et al. 2022) revealed FF waves in the 30–50 Hz range and FB waves in the 3-6 Hz range, where the phase of the FB oscillations modulated the amplitude of the FF oscillations. However, this was the only study on mice, to the best of my knowledge, that has investigated the FF-FB waves in the visual system. Additionally, the study utilized a simple visual stimulus that did not involve any prediction and higher-level cognitive processes.

The mouse visual system offers several advantages for studying predictive coding. The simpler and well-studied visual processing hierarchy in mice allows for more straightforward analysis of neural data. Genetic manipulation tools in mice also provide unique opportunities to explore cortical micro-circuitry and manipulate neural pathways, which is challenging in primates. Additionally, mouse studies are more cost-effective and logistically feasible compare to primates, making them an attractive model for large-scale explorations of complex brain functions like predictive coding.

The International Brain Laboratory (IBL) (Benson et al. 2023) provides an extensive open-access dataset recorded from more than 100 mice trained to perform a perceptual decision-making task. In this task, mice are presented with a visual stimulus of controlled contrast and are required to move the stimulus to the center of the screen using a steering wheel. The stimulus appears on the right or left side of the screen, with a fixed probability for blocks of trials to create a predictable pattern. Yet, these bias blocks change unpredictably, requiring the mice to constantly update their predictions and internal model of the environment. Therefore, this sophisticated experimental paradigm provides a valuable opportunity to study the neural implementation of predictive coding.

1.2   Current project

To date, IBL researchers have primarily focused on detecting, sorting, and analyzing action potentials and firing rates, without prioritizing a specific brain region or cognitive process. The overarching goal of the current project is to go beyond their data-driven analyses and to use the IBL dataset as a benchmark to study the neural implementation of predictive coding in the mammalian brain. In this perspective, we were particularly interested in local field potentials (LFP) and oscillatory electrophysiological signals in the theta (typically, between 2 to 7 Hz), alpha (7 to 15 Hz), beta (15 to 30Hz) and gamma (30 to 200Hz). Until recently, LFPs recorded in the IBL context have been left almost unexplored and the analysis of LFP signals produced by Neuropixel probes (as used by all IBL experiments) has received limited attention (Windolf et al. 2023).The current project represents a first step towards unlocking the great potential of the IBL dataset to constrain theories of predictive

coding and communication through oscillations in the brain.

Thus, the primary goal was to assess the quality and usability of IBL LFP data through a careful development of preprocessing pipelines and the comparison of different artifact detection and signal re-referencing methods. The second goal was to confirm that a core principle of communication through oscillations could be observed in the dataset. To reach this goal, I performed the following analysis: 1) The inter trial phase coherence (ITC) analysis, as it reflects the degree of temporal synchronization in response to sensory stimuli. 2) Time frequency analysis to examine the dynamic change in high and low frequency ranges over time, given that they are indicators of FF and Fb communications, respectively. 3) Analyzing phase amplitude coupling (PAC) in order to quantify the degree to which the phase of low frequency oscillations modulates the amplitude of high frequency waves. Growing evidence claim this cross frequency interaction facilitate communication within the brain during sensory processing [Bonnefond and Jensen (2015); (**seymo?**)

2 Methods

2.1 Data recording details

2.1.1 Task detail

In the IBL task (Figure 1a,b), head-fixed mice had to move a visual stimulus to the center by turning a wheel with their front paws. At the start of each trial, the mouse was required to refrain from moving the wheel for a quiescence period lasting between 400 and 700 milliseconds. After this period, a visual stimulus (Gabor patch) appeared on either the left or right side of the screen accompanied by a 100-millisecond tone (5 kHz sine wave). If the mouse correctly moved the stimulus to the center by turning the wheel over 35°, it received a 3 µL water reward. Incorrect responses or failing to respond within 60 seconds resulted in a 500-millisecond burst of white noise and a timeout (Benson et al. 2023). As shown in Figure 1c, mice typically responded quickly mainly within 2 seconds. The stimulus is always presented for the first 1 second regardless of response time (RT). RT is defined as the time after stimulus when the wheel rotation exceeds the threshold.

The experiment began with 90 unbiased trials where the stimulus appeared equally on both sides. The stimulus contrast levels were presented in a ratio of [2:2:2:2:1] for contrasts [100%, 25%, 12.5%, 6%, 0%]. After this initial block, trials were organized into biased blocks where the likelihood of the stimulus appearing on one side was fixed at 20% for the left and 80% for the right in "right blocks"

or vice versa in "left blocks." These blocks consisted of 20 to 100 trials determined by a truncated geometric distribution with stimulus contrast levels ratio identical to those in the unbiased block. In 0% contrast trials where no stimulus was visible, the side assignment followed the block bias (e.g., right side for right blocks) (Benson et al. 2023).
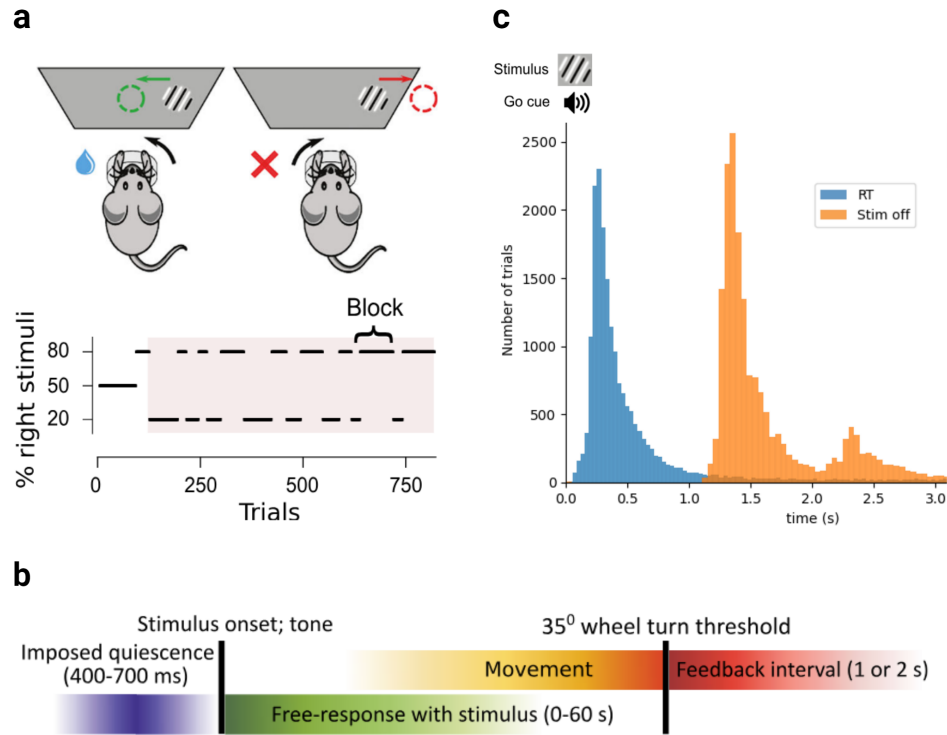

Figure 1: **International Brain Laboratory (IBL) task. a)** Example session block diagram and IBL task. Each block of consecutive trials after 90 trials varied the probability of the stimulus being on the right side. **B)** A timeline of the main events and variables of the IBL task. After a quiescence period, stimulus appears on screen alongside a go cue tone. Mice had to bring the stimulus to the center by turning the wheel. When the wheel rotation reaches the threshold 35 ° or after 60 s of no response, positive or negative feedback is provided depending on the mice choice. (a) and (b) panels are extracted from (Benson et al. 2023). **C)** Distribution of response time (RT) with color blue and stimulus offset time with color yellow relative to stimulus onset. Note that there is always a stimulus presented for the first 1 second even though the mice typically answer sooner.

2.1.2   Electrophysiological recording

The neural recordings were conducted using Neuropixel probes with 384 recording channels and 960 low-impedance sites on a single shank (Benson et al. 2023). Neuropixel probes are advanced silicon-based neural recording devices designed for high-density recording of neural activity across large populations of neurons with precise spatial and temporal resolution (Jun et al. 2017). Data are collected from 267 brain regions by inserting 547 Neuropixel probes covering most of the left hemisphere. After the recordings, electrode tracks were reconstructed by performing serial-section 2-photon microscopy. A region was then assigned to each recording site (and inferred single neurons) within the Allen Common Coordinate Framework (Benson et al. 2023).

2.2   Preprocessing of electrophysiological data

2.2.1   Exclusion of channels and trials

Local field potential (LFP) datasets, along with their corresponding behavioral data and channel locations, were extracted for sessions that included at least one channel in the primary visual cortex. The destriping function of the IBL Python toolbox was applied as the first step of preprocessing to correct for the biases induced by the sequential acquisition of the raw voltage traces (IBL 2024). This was followed by downsampling from 1000 Hz to 500 Hz to decrease the size of the data files. Next, channels were excluded based on three criteria: (i) those not located in the primary visual cortex (ii) those displaying excessively high variance according to power spectral density (iii) and those with excessively low coherence with neighboring channels.

We faced an unexpected problem with IBL LFP data due to amplifier saturation. Indeed, Neuropixel probes (especially the earlier version) have a limited dynamic range that was frequently exceeded during the task (in particular, when the animal licked the spout to harvest water reward). For the analysis of spikes, this issue is less problematic as it only prevents detecting spikes during saturation. However, for the analysis of LFP, it introduces very salient artifacts and dramatically increases inter-trial variance in power, amplitude, and phase estimates, potentially leading to erroneous conclusions. Therefore, we designed a custom exclusion procedure tailored to capture this specific problem. Trials were excluded based on the skewness of the absolute value of their first-order temporal derivative (threshold set to 1.5). Indeed, high skewness values typically reflect the presence of sudden, large amplitude changes in an otherwise mostly flat signal. By excluding these trials, our analyses focus on more consistent and representative portions of the data, improving the reliability of the results. All

remaining trials were included in the presented analyses (i.e., missed, incorrect and slow responses). Lastly, sessions were excluded from further analysis if they had more than 40% noisy channels or trials.

2.2.2 Common average reference

Our electrophysiological analyses used a common average reference scheme. The common reference was recomputed as the mean of all channels of interest per animal (i.e., those located in the primary visual cortex), after excluding noisy channels). This approach was chosen to limit the influence of electrical potentials outside of visual areas as well as the influence of non-physiological noise.

2.3 Time-Frequency analysis

For the time-frequency analysis, we chose the multitaper method. This method is known to be well-suited for situations where specific frequency bands are not preselected and the goal is a broad exploration of all frequencies. Multitaper parameters were selected in a way where frequency resolution was prioritized slightly over temporal resolution, especially at lower frequencies. In this regard, power and phase were calculated using MNE's multitaper function(Gramfort et al. 2013) with the following parameters: a frequency range of 2-45 Hz with a step size of 0.5 Hz for the 2-10 Hz range and 1 Hz for frequencies above 10 Hz and a time-bandwidth product of 3.5 with the number of cycles at each frequency point set to half of the corresponding frequency (n-cycles $= \frac{f}{2}$). These parameters were found to be optimal for our specific data and goals.

Baseline correction were applied to the time frequency data with baseline defined as the interval from -0.7 to -0.5 seconds relative to stimulus onset. For baseline correction, the percentage change method were used which can be expressed with the following formula:

$$\text{Corrected Power}(t, f) = (\frac{P(t, f) - \text{Baseline}(f)}{\text{Baseline}(f)}) \times 100$$

Where $P(t, f)$ is the power at a specific time (t) and frequency (f), and $\text{Baseline}(f)$ is the averaged power within the baseline interval for each frequency.

2.4 Inter trial Phase coherence (ITC)

Inter-trial phase coherence (ITC) was computed using MNE's built-in function. ITC is a measure of the consistency of the phase of a signal across different trials at a given time and frequency. Mathematically, ITC is calculated as the magnitude of the average of normalized complex phase values across trials. For each trial, the phase of the signal, denoted as $\phi(f, t)$, is extracted at each frequency f and time point t. These phase values are then represented as unit vectors on the complex plane, i.e., $e^{i\phi(f,t)}$.

The ITC at a particular time-frequency point is then defined as:

$$\text{ITC}(f, t) = \left| \frac{1}{N} \sum_{n=1}^{N} e^{i\phi_n(f,t)} \right|$$

where N is the number of trials, and $\phi_n(f, t)$ is the phase at frequency f and time t for the n-th trial. The resulting ITC value ranges from 0 to 1, where 0 indicates no phase consistency across trials, and 1 indicates perfect phase alignment across all trials.

2.5 Phase-Amplitude Coupling

Phase-Amplitude Coupling (PAC) quantifies the interaction between the phase and amplitude of two distinct frequency bands, typically involving the phase of a low-frequency oscillation and the amplitude of a high-frequency oscillation. In this study, PAC was computed for phase frequencies ranging from 2 to 5 Hz and amplitude frequencies from 25 to 80 Hz using the TensorPAC Python module (Combrisson et al. 2020). The process begins with the extraction of the instantaneous phase of the low-frequency signal and the amplitude envelope of the high-frequency signal carried out through Morlet wavelets. The interaction between these signals is then evaluated to determine how the phase of slower oscillations modulates the amplitude of faster oscillations. In this project, the Gaussian Copula (GC) method was employed to compute PAC for a time window spanning 500 ms before stimulus onset to 1 second after the stimulus. Compared to other methods such as Phase Locking Value, GC is more robust to shifts in overall signal amplitude (Combrisson et al. 2020).

The core of the GC method involves calculating the mutual information between normalized amplitude and phase to quantify the degree to which the phase of the low-frequency oscillation governs the amplitude of the high-frequency oscillation. This mutual information provides a lower-bound

estimate of the PAC that is robust to overall amplitude shifts. Mathematically, this can be expressed as:

$$gcPAC = I(a(t); \sin(\phi(t)), \cos(\phi(t)))$$

Where I denotes the mutual information, $a(t)$ represents the normalized amplitude signal, and $\phi(t)$ represents the normalized phase signal.

After computing PAC, the values were normalized for each channel using z-score normalization, which involves subtracting the mean and dividing by the standard deviation. This process standardizes the PAC values and makes them comparable across channels and subjects. Following normalization, the values were averaged across all frequencies and for two distinct time windows: before the stimulus (-0.5 to 0 seconds) and after the stimulus (0 to 1 second).

2.6 Statistical Analysis

2.6.1 Cluster based permutation

To identify significant clusters in the ITC estimates, we employed the one-sample permutation cluster test, as implemented in the MNE-Python library (Gramfort et al. 2013). The use of permutation tests is particularly crucial in this context due to the multiple comparison problem inherent in time-frequency analyses, where statistical tests are conducted across many time points and frequency bands. Without proper correction, this can lead to a high rate of false positives (Type I error) . Traditional methods of controlling for multiple comparisons, such as the Bonferroni correction, tend to be overly conservative, potentially reducing statistical power and increasing the likelihood of false negatives (Type II errors). Permutation tests provide a non-parametric solution to this problem. They make no assumptions about the distribution of the data, making them particularly suitable for neurophysiological data, which often do not follow normal distributions. Instead of relying on theoretical distributions to determine significance, permutation tests use the data itself to empirically construct a null distribution. This approach allows for accurate control of the family-wise error rate (FWER) while maintaining higher sensitivity in detecting true effects (Maris and Oostenveld 2007; Sassenhagen and Draschkow 2019).

In our analysis, we used 1000 permutations to generate the null distribution. The permutation test works by randomly shuffling the data labels and recalculating the test statistic (in this case, the t-statistic) for each permutation. This process is repeated many times (1000 in our case), and for

each permutation, the maximum t-value across all time-frequency points is recorded. This set of maximum t-values forms the null distribution. The significance threshold is then defined based on this null distribution. Specifically, the threshold is set to a value that corresponds to the desired alpha level (0.05), ensuring that the probability of observing a cluster of significant time-frequency points under the null hypothesis is appropriately controlled. By setting the threshold to None, we allowed MNE-Python to automatically compute this threshold based on the distribution of maximum t-values from the permutations, ensuring that the threshold is data-driven and adapted to the observed data distribution. Clusters of time-frequency points that exceed this threshold are considered statistically significant, indicating that the observed ITC values in these clusters are unlikely to have occurred by chance. However, it's important to note that cluster-based statistics do not provide a straightforward method for computing effect size. In another words, these test can indicate where significant effects occur, but they do not readily measure the magnitude or strength of those effects.

2.6.2   Friedman Test and Repeated measures ANOVA

To statistically evaluate the effects of stimulus contrast on averaged ITC and theta-gamma power, we employed the Friedman test, a non-parametric alternative to repeated measures ANOVA. This choice was made because the data did not follow a normal distribution, as confirmed by the Shapiro-Wilk test. Following the Friedman analysis, we conducted a Nemenyi post-hoc test to further explore the pairwise group effects. Additionally, to assess whether the PAC distribution differed significantly before and after stimulation, we utilized repeated measures ANOVA, which was appropriate as data had a distribution.

3   Results

3.1   Data summary

A total of 63 probes were identified in the IBL datasets, with at least one channel assigned to the primary visual cortex (V1) (see Figure 2a;b for one insertion example). From the initial dataset, 7 and 15 insertions were excluded due to over 40% noisy channels and trials, respectively. In the end, 41 insertions (subjects) were retained, consisting of 2,262 total channels and 25,075 trials. On average, each probe was associated with 54.83 channels in V1 (range: 2 to 118), with an average of 532.66 trials per session (range: 276 to 1,098) (see Figure 2d.) Among the total number of channels, 212 (9.37%) were in layer 1, 456 (20.16%) in layer 2/3, 338 (14.94%) in layer 4, 650 (28.74%) in
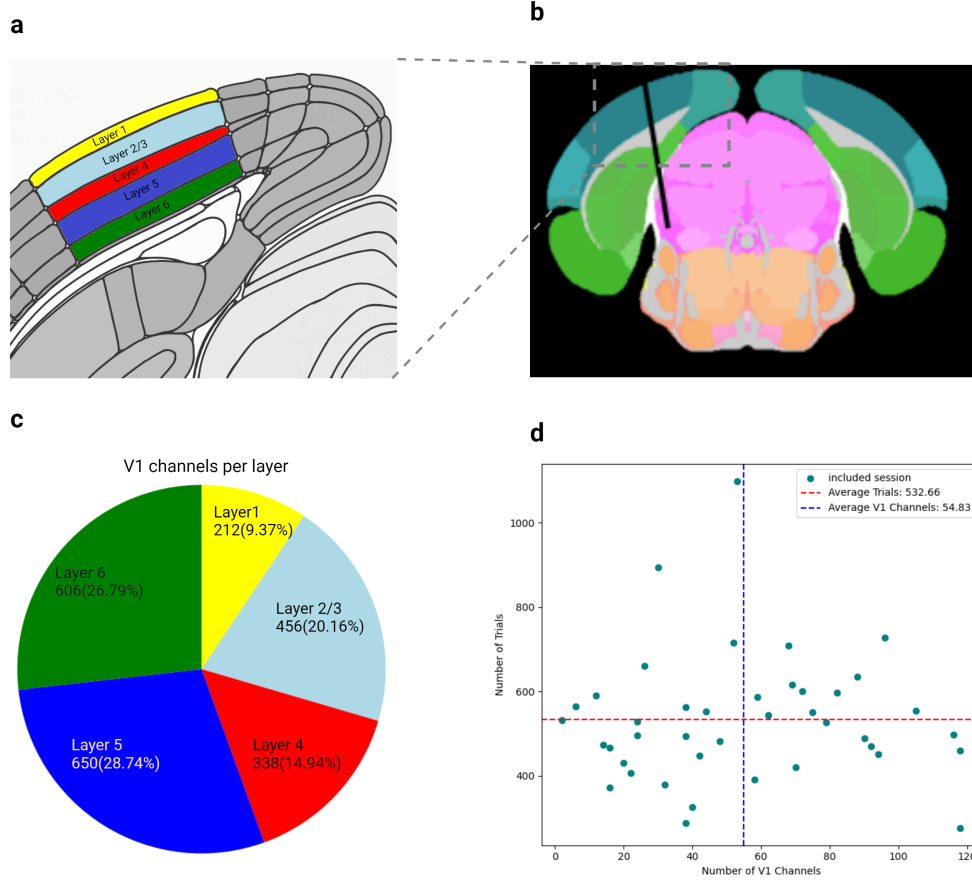
layer 5, and 606 (26.79%) in layer 6 (see fig X c).

Figure 2: **Region of interest and recording site locations. a)** Coronal slice of the Allen Brain Atlas, highlighting the layers of the primary visual cortex (V1) with distinct colors: yellow for layer 1, light blue for layers 2/3, red for layer 4, blue for layer 5, and green for layer 6. The image base is extracted from the Allen Brain Atlas (https://atlas.internationalbrainlab.org) at an Anterior-Posterior (AP) coordinate of -3140 μm. **b)** Coronal slice from the Allen Brain Atlas that shows an example of a probe insertion site in a mouse brain (subject name: NYU-12). The black line represents the probe path, starting in V1 and ending in the midbrain reticular nucleus (approximately). The image is taken from the IBL online data visualization tool (https://viz.internationalbrainlab.org). **c)** Pie chart illustrating the proportional distribution of each V1 layer, using the same color scheme as in panel (a). **d)** Scatter plot showing the number of trials (range: 276-1098) and channels (range: 2-118) for the included sessions. The mean number of channels (54.83) is indicated by a dashed blue vertical line, and the mean number of trials (532.66) is represented by a dashed red horizontal line.

3.2 Behavioral results

In line with previous results on whole sessions, mice performed correctly on 80.7% ± 5.8% (mean ± s.d.) of the trials with reaction time (RT) of 1.73 ± 5.7 seconds (mean ± s.d.). RT is defined as the time interval between stimulus onset and when wheel rotation reach threshold of 35° ; and performance is computed as a percent of correct trials over total number of trials. As illustrated in (Figure 3 a;b), Performance improved and reaction times decreased on trials with higher stimulus contrast. In 0% contrast trials, where mice had to rely only on their expectation and prior experience, they made correct choices in 57% ± 8% (mean ± s.d.).
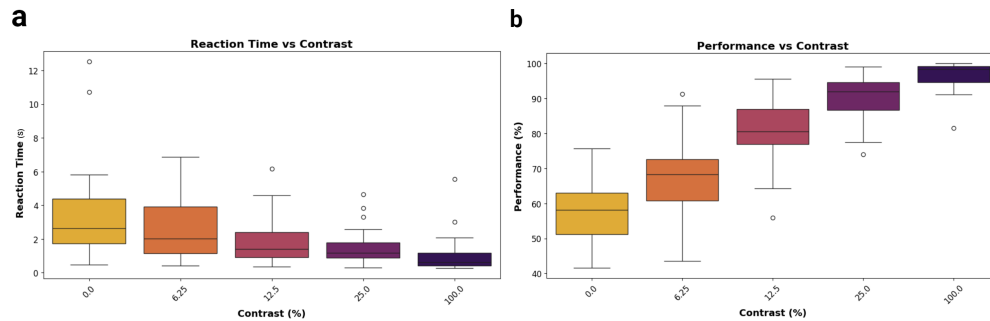

Figure 3: **Behavior results. a)** Illustration of reaction time for different stimulus contrast level using boxplot. **b)** Illustration of performance (as a percent of correct trials over total number of trials) for each contrast levels using boxplots. For both (a) and (b): number of subject (N= 41), the central line in each box indicates the median value, while the box edges represent the inter-quartile range (IQR) and whiskers extend to 1.5 times the IQR.

3.3 Inter trial phase coherence (ITC)

The ITC analysis indicated significant phase alignment in the theta frequency band (2-5 Hz) within the [0, 0.5] second interval following the stimulus (see Figure 4a). To ensure that these findings were not due to chance and to correct for multiple comparisons, we applied the MNE one-sample cluster permutation test. The significant clusters, marked by the black line in Figure 4a, demonstrate that the low-frequency ITC during the 0-0.5 second period was statistically meaningful, with a p-value of 0.001. Additionally, as illustrated in Figure 4c, there were no significant differences in ITC across the V1 layers in the low-frequency range.

To assess whether the observed ITC levels were influenced by the stimulus, ITC average levels were compared for each level of stimulus contrast. The average ITC was computed for the low-frequency

range (2-8 Hz) and within the 0-0.5 second time window post-stimulus. As illustrated in Figure 4b, an increase in stimulus contrast generally resulted in a higher mean ITC. Interestingly, the only group of trials that did not support this trend was trials without stimulus (i.e. contrast 0%), which with more detail will be addressed in discussion.

To statistically evaluate whether the mean ITC was significantly affected by contrast levels, further analysis was undertaken. Given that the Shapiro-Wilk normality test did not confirm normality in the data distribution, the Friedman test, a non-parametric alternative to repeated measures ANOVA, was employed. The results of the Friedman test revealed a highly significant effect of contrast level on ITC mean, ($\chi^2(4, N = 200) = 77.98$, p-value = 4.66 x$10^{-16}$), indicating that variations in ITC across different contrast levels were unlikely to have occurred by chance. Due to the significant effect of contrast level on ITC mean identified by the Friedman test, a post-hoc Nemenyi test was performed to determine which specific contrast levels contributed to the observed differences. The Nemenyi test was chosen as it is appropriate for pairwise comparisons following a Friedman test. The post-hoc analysis results are presented in Figure 4d, with p-values indicating the significance of differences between each pair of contrast levels.
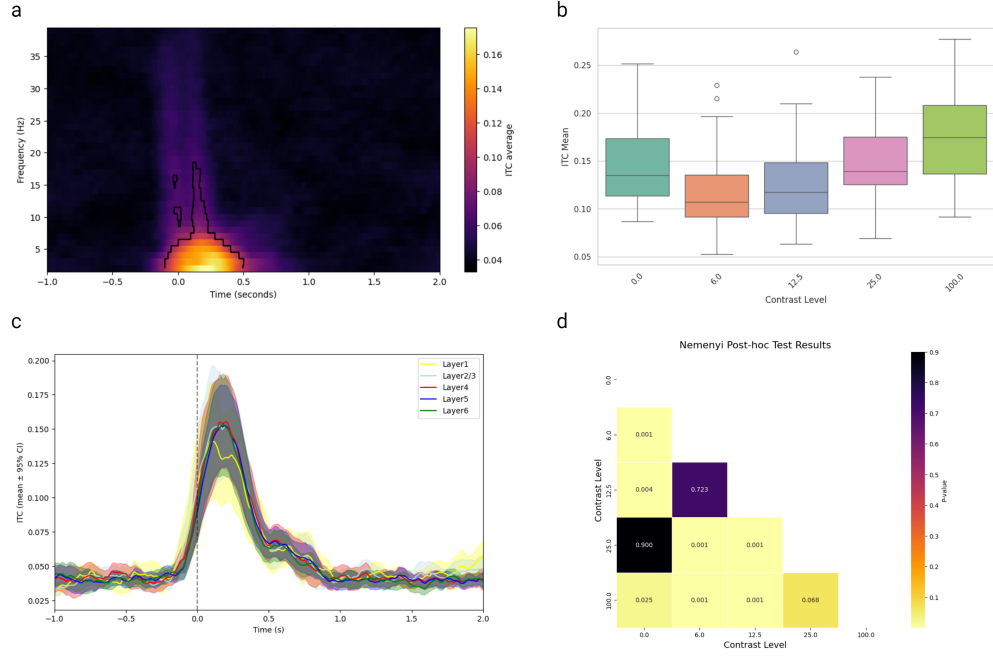
Figure 4: **Inter trial phase coherence (ITC). a)** ITC average across all subjects and cortical layers relative to stimulus onset. Significant clusters (p = 0.001, N=41) are indicated by black lines, as determined by the MNE one-sample cluster permutation test. **b)** Comparison of ITC averages across different stimulus contrast levels using a box plot. The ITC average was computed for the 2-8 Hz frequency range within the 0-0.5 second time window post-stimulus, aggregated across all subjects and layers. The central line in each box indicates the median ITC average value, while the box edges represent the inter-quartile range (IQR) and whiskers extend to 1.5 times the IQR. **c)** Low-frequency ITC averages for each V1 layer relative to stimulus onset. The layer-specific averages are depicted with solid lines, and their 95% confidence intervals are shaded around the lines in distinct colors: yellow for layer 1, light blue for layers 2/3, red for layer 4, blue for layer 5, and green for layer 6. **d)** Nemenyi post-hoc test p-value results for each pair of contrast levels. Lower p-values indicate significant differences between the ITC average distributions for each pair, represented by a heatmap ranging from yellow (low p-values) to black (high p-values).

3.4 Time frequency analysis results

Although there was substantial variability across subjects, the time-frequency analysis of V1 revealed two notable oscillations in relation to the visual stimulus: first, an increase in high-frequency power within the low-gamma band range (20–40 Hz), and second, a concurrent decrease in theta power (2–5 Hz) . The low-gamma increase was more transient, while thetheta inhibition persisted for a longer duration (see Figure 5). As shown in Figure 6a,b, the observed frequency band changes exhibited a similar pattern across the different layers of V1. Statistical tests were not applied to quantitatively

evaluate the layer-specificity of these effects, as the variability in the number of channels across layers and subjects did not allow for such an analysis.

The averaged power of each frequency band over the first 1 second after the stimulus was compared for trials with different contrast levels. The Friedman test revealed a statistically significant effect of contrast level on power modulation in both the theta ($\chi^2(4, N = 200) = 20.54, p = 0.000391$) and the low-gamma ($\chi^2(4, N = 200) = 18.88, p = 0.000830$), indicating that power in these bands was significantly influenced by the stimulus contrast. However, as you can see in Figure 7a,b, the frequency band average power across different contrast levels is not quite observable. Additionally, the post-hoc test results shown in Figure 7c,d indicate that the comparisons were mainly significant only in comparison to the 100% contrast condition.

This not readily observable difference is believed to be mainly due to inter-subject variability, with some subjects showing significant contrast-related modulations, while others do not. In general, especially in sessions with high effects of contrast on power bands, higher contrast stimuli involved greater increases in low-gamma and decreases in theta band power.
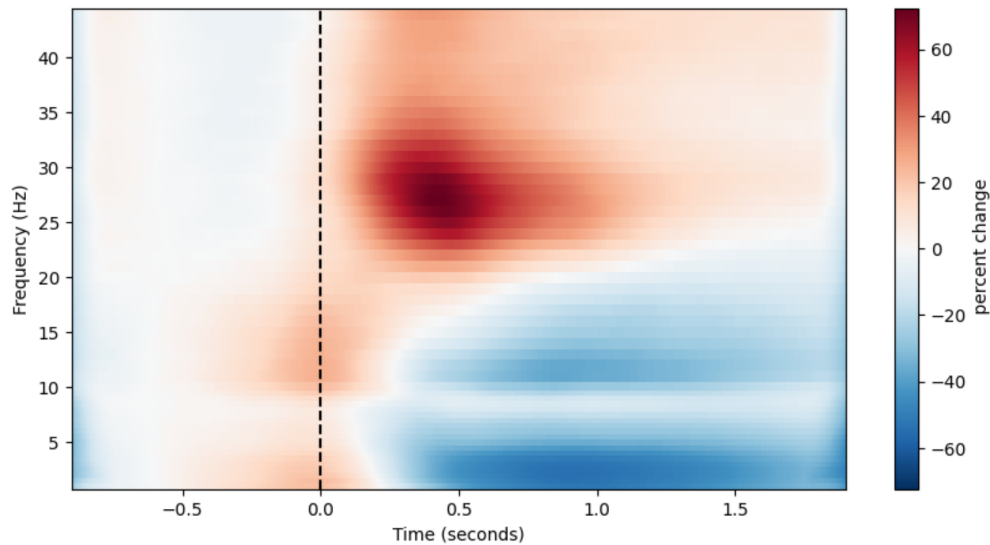

Figure 5: **Average time frequency representation.** Time-frequency is averaged over all channels in the primary visual cortex, computed using the multitaper method. The data is baseline-corrected using the -0.7 to -0.5 s pre-stimulus interval, with time relative to stimulus onset (marked by dashed black vertical line). Power is shown in percent units with a blue-to-warm colormap.
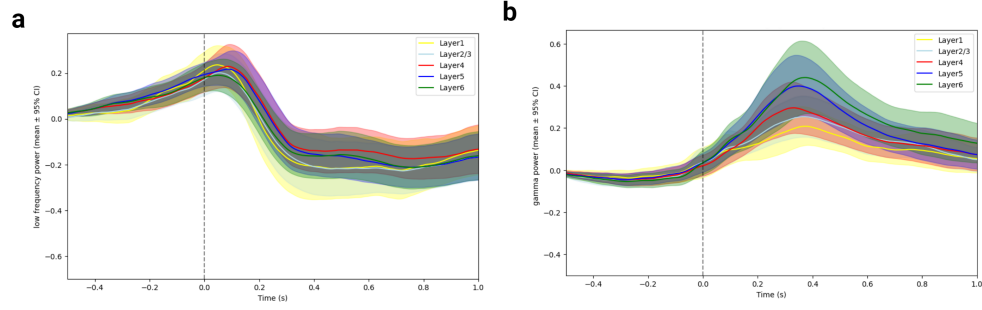
15

Figure 6: **Average frequency band power across time for all layers of V1**. **a)** low frequency (2-5 Hz) average power for each V1 layer relative to stimulus onset (marked by dashed black vertical line). The layer-specific averages are depicted with solid lines, and their 95% confidence intervals are shaded around the lines in distinct colors: yellow for layer 1, light blue for layers 2/3, red for layer 4, blue for layer 5, and green for layer 6. **b)** similar to panel (a) but for higher frequency band (20-40 Hz). The separation by layer is for visual purpose only (no statistical tests applied).
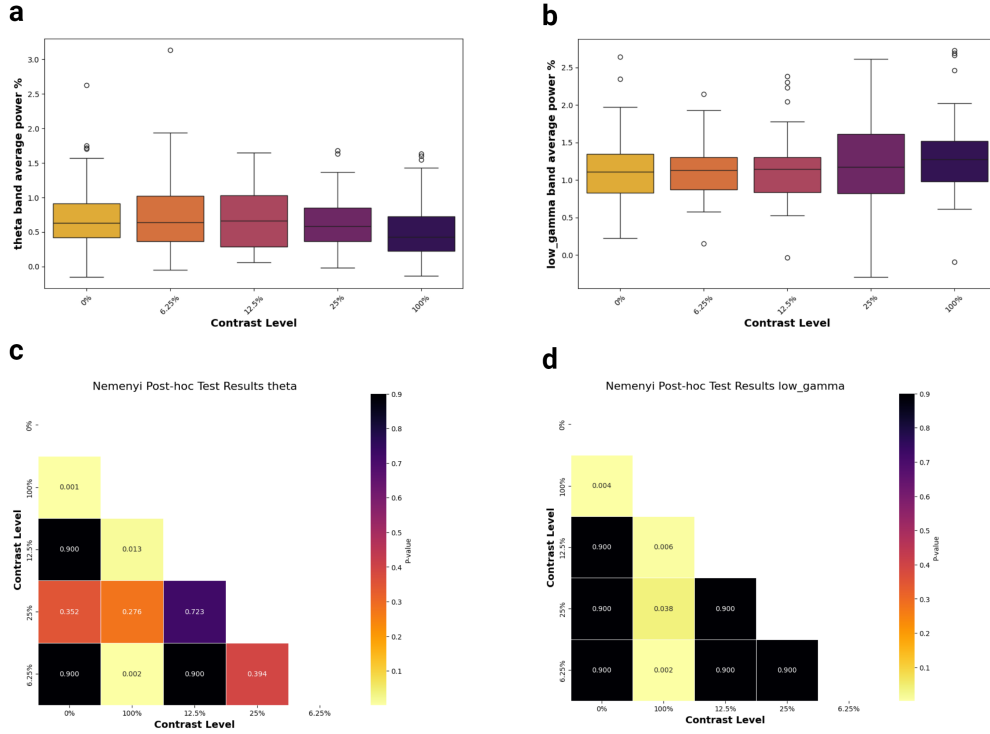
Figure 7: **Affects of stimulus contrast on low and high frequency average power. a)** The box plots represents the distribution of low-frequency (2-5 Hz) average power across different contrast levels.The power is averaged over the first 1 second after stimulus across all channels of each subject (N= 41). The central line in each box indicates the median power average value, while the box edges represent the inter-quartile range (IQR) and whiskers extend to 1.5 times the IQR. **b)** similar to panel (b) but for high frequency range (20-40 hz). Note that the error bars of (a) and (b) reflect inter-individual variability whereas the statistical inference of interest involve a within-subject factor (contrast). **c)** Nemenyi post-hoc test p-value results comparing low frequency average power for pairwise contrasts levels. Lower p-values indicate significant differences between the low frequency average power distributions for each pair, represented by a heatmap ranging from yellow (low p-values) to black (high p-values). **d)** similar to panel (c) but for high frequency (20-40 Hz) average power.

3.5 Phase amplitude coupling (PAC)

Phase-amplitude coupling (PAC) analysis revealed that the phase of theta oscillations (2-5 Hz) modulates the amplitude of high-frequency oscillations (25-80 Hz). In Figure 8, an example from a single channel illustrates how the amplitude of high-frequency oscillations changes depending on the phase of theta oscillations during the period after the stimulus. This example visually demonstrates

the coupling effect; however, it is important to note that this figure serves solely as an illustration of the amplitude modulation by phase, and no specific coupling method (e.g., Gaussian copula) was applied to quantify this effect.
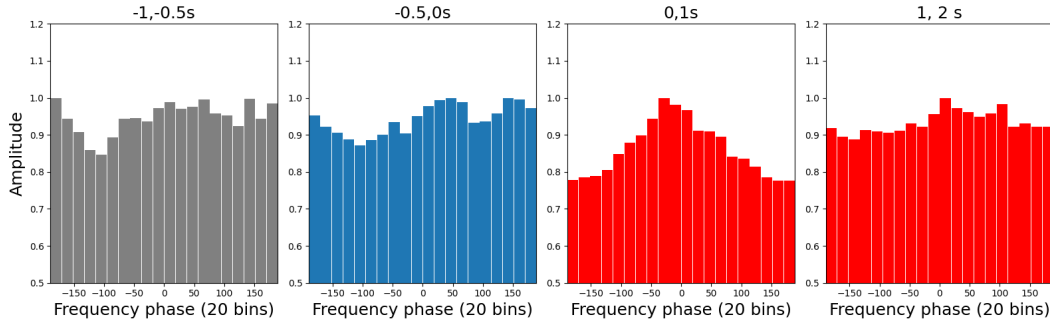

Figure 8: **Binned Amplitude by Phase for a channel in V1**. This figure illustrates the binned amplitude of high-frequency oscillations (25-80 Hz) as a function of the phase of theta oscillations (2-5 HZ) for four time windows. From left to right : (-1, -0.5), (-0.5, 0), (0, 1), and (1, 2) with time in seconds relative to the stimulus onset. The data were binned into 20 equal-sized phase bins, and the amplitude was averaged within each bin. The non-uniform distribution of amplitudes indicate high possibility of coupling. As you can see, the time period one second after stimulus (0, 1s) shows observable non-uniform distribution of amplitudes with the highest value for phase zero. This plot is intended to illustrate the relationship between phase and amplitude without applying any coupling quantification. The plot is made using Tensorpac python module (Combrisson et al. 2020).

Comparing PAC values for the time periods before and after the stimulus revealed a significant increase in PAC values following the stimulus. This difference was confirmed by a repeated measures ANOVA, which resulted in $F(1, 39) = 5.503$, $p = 0.0242$. The distribution of average PAC values before the stimulus was centered slightly towards negative values (mean: -0.05) and exhibited large tails in both positive and negative directions (standard deviation: 0.05). In contrast, the distribution of PAC values after the stimulus was centered on positive values (mean: 0.02) with narrower tails (standard deviation: 0.01) (see Figure 9a).

In addition, we found that this difference between PAC values were more pronounced in layer five and six (see Figure 9b). As illustrated in Figure 10, these two V1 layers were the only layers with F values higher than F-critical (approximately 4). However , similar to Time frequency analysis, no further statistical tests were applied to quantitatively evaluate the layer-specificity due to the variability in the number of channels across layers.
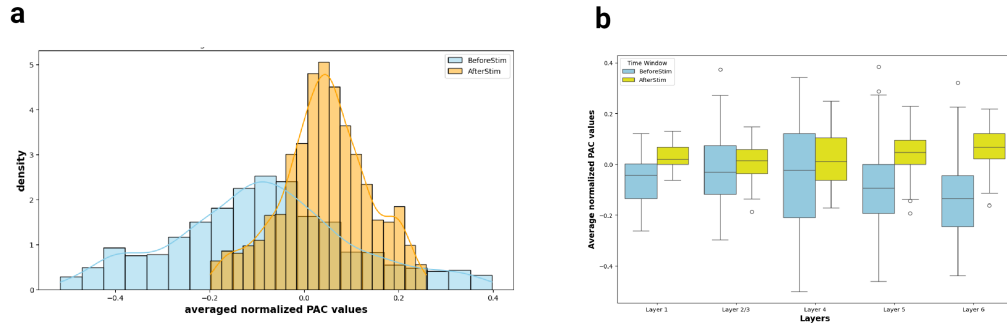
Figure 9: **Phase Amplitude Coupling (PAC) values before and after stimulus. a)** Histogram distribution of averaged normalized PAC values for frequency of phase (2-5 HZ) and frequency for amplitude of (25-80 HZ). The distribution is across all V1 channels (N = 2,262) and for two time period: after stimulus (0-1 s) with color yellow and before stimulus (-0.5, 0 s) with color light blue. The histograms are computed with 20 bins, and a kernel density estimate (KDE) is overlaid with solid line. **b)** Boxplot illustration of before (yellow) and after (light blue) stimulus PAC values for each layer of V1, with number of channels per layer : layer1 = 212, layer 2/3: 338, layer 4 = 650, layer 5 = 650, layer 6 = 606. As you can see the difference is significant mainly in layer 5 and 6.
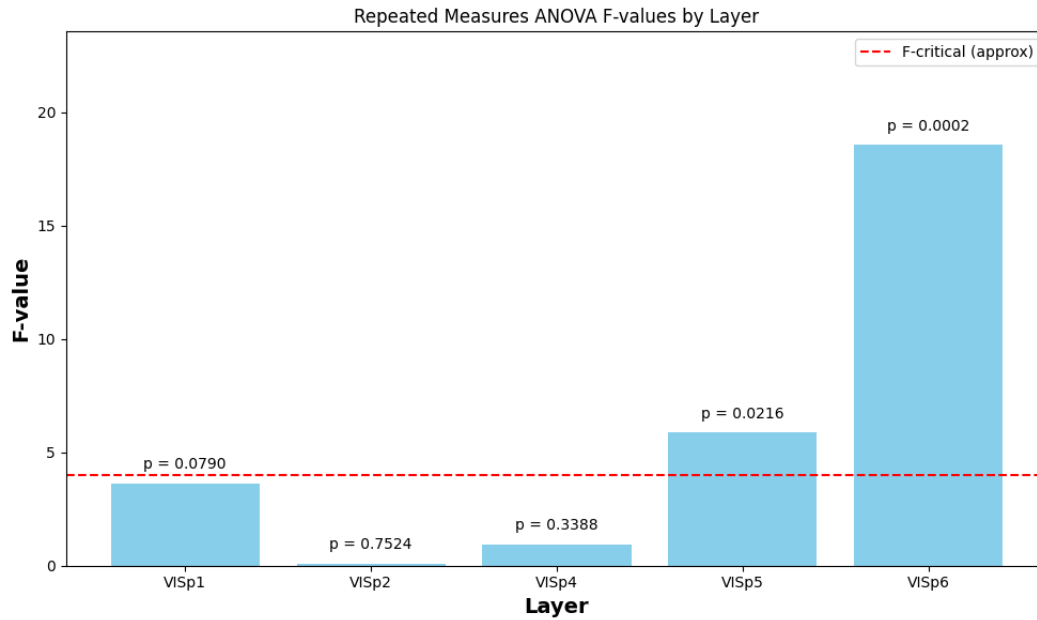

Figure 10: **Repeated measure ANOVA F-values per layer.** Each V1 layer is indicated by VISp (n) where n is the number of layer. This plot shows that only layer 5 and 6 had F-value over the F-critical approximation (4, marked by dashed horizontal line).

19

4   Discussion

According to predictive coding and communication by oscillations theories, high-frequency feedforward (FF) and low-frequency feedback (FB) oscillations may contribute to the hierarchical processing of sensory stimuli by generating predictions and attaching behavioral context to the sensory world (Aggarwal et al. 2022). Yet, the role of these oscillations in shaping perception remains poorly understood, particularly in mice. The International Brain Laboratory (IBL) open-access datasets, with their sophisticated experimental paradigms and large-scale neural recordings, provide an unprecedented opportunity to study the principles of predictive coding in mice. In this project, we analyzed the IBL local field potential data from the primary visual cortex (V1) as a first step towards utilizing this dataset to understand the principles of predictive coding and communication through oscillations.

The inter trial phase coherence (ITC) analysis revealed a significant theta (2-5 Hz) phase coherence within the first 500 ms after visual stimulation. This frequency and temporal range of observed phase coherency is totally consistent and similar to previous study in mice (Aggarwal et al. 2022). The time frequency (TF) analysis showed an increase in low gamma (25-40 HZ) power with concurrent decrease of theta power after visual stimulation. Consistent with presumed FF-FB roles of these high and low frequency band power we found shorter and transient peak in low gamma with longer lasting theta decrease. In addition, these results add evidence to the previous line of thought Senzai, Fernandez-Ruiz, and Buzsáki (2019) that suggests the functional properties of theta oscillations in mice are analogous to primate alpha oscillations (7-15 HZ), including an anti correlation with local firing rate and decreased power upon visual stimulation.

By statistically analyzing the effects of stimulus contrast on ITC and TF results, we further confirmed that the observed pattern is significantly dependent on contrast, a key property of any visual stimulus. One interesting observation was that in trials without any stimuli, the theta dynamics in both ITC and TF did not follow the linear trend established by non-zero stimulus contrasts. For example, in analyzing theta phase coherency with respect to stimulus contrast, the common trend is a decrease in coherency as contrast decreases. Yet, the 0 contrast trials surprisingly showed higher coherency, closer to the higher contrast condition. Considering theta dynamics as a signature of feedback communication, we believe this observation could possibly indicate the presence of two different FB signals. For instance, the theta ITC (2-8Hz) for zero contrast could be related to an surprise FB signal because the mouse has heard the go cue tone, while the theta ITC when there is a stimulus could be an FB signal from higher-order areas related to the complex features of the stimuli. As the mouse

cannot see the low-contrast stimuli well, this FB signal is lower, leading to less theta ITC. This line of reasoning is only valid if we accept that the theta ITC/TF pattern in no-stimulus trials is not related to noise. Another, simpler possibility is that effortful perception at lower contrast leads to an increase in visual attention, which is known to induce decreased alpha power dynamics in primates (i.e., theta in mice)(Bollimunta et al. 2008).

The phase amplitude coupling (PAC) analysis showed significant theta-low gamma coupling after visual stimulation. This finding aligns with a previous study in mice (Aggarwal et al. 2022) and is analogous to alpha-gamma coupling observed in primates during sensory processing (Spaak et al. 2012). Although this result adds important value to this line of evidence, further analysis is needed to determine the degree to which we can relate this PAC to task features. Similar to our previous investigations of ITC and TF, we can start by analyzing how the contrast of stimuli affects PAC, then extend the analysis to include other task variables such as the bias block, expected versus unexpected stimuli, and correct versus incorrect trials. Additionally, an important consideration for future PAC studies is to apply correction methods, such as using surrogate null distribution, to mitigate the randomly driven and noise-driven coupling inherent in PAC analysis.

Contrary to our expectations, we did not observe layer-specific differences in the different frequency bands. The use of a unipolar montage may explain the lack of layer-specific differences we observed, as this approach can reduce spatial specificity due to the volume conduction effect. To address this issue, we computed current source density, but this led to increased noise and channel variability, making it challenging to aggregate the data. For future studies, we suggest using an intermediate method, such as near-field LFP (Tovar et al. 2023), to better balance the preservation of both local and overall voltage fluctuations.

4.1   Limitations and further studies

While our study provided valuable findings, we acknowledge two significant limitations. First, our analysis was confined to the primary visual cortex, which, although a good starting point, does not capture the full complexity of visual processing in the brain. Expanding our analysis to include higher-order visual areas could allow us to explore inter-regional communication. This is particularly critical for understanding FF and FB signals, which are better interpreted in the context of interactions between lower-level and higher-level cortical areas. Second, our study primarily utilized the contrast variability of stimuli from the sophisticated task paradigm provided by the IBL. While

this approach yielded meaningful results, it did not fully leverage the complexity of the experimental design, particularly aspects related to prediction and expectation. Incorporating more complex variables, especially those related to predictive coding, could significantly enhance our understanding of neural oscillations in predictive coding. For instance, future studies could analyze oscillatory activity in relation to conditions where stimulus is expected versus unexpected

4.2 Conclusion

In conclusion, this project made a significant step towards leveraging the IBL dataset to explore the neural mechanisms of predictive coding in the mammalian brain. First, we showed that despite unexpected artifacts due to amplifier saturation in IBL LFP data, careful selection of preprocessing procedures make these datasets well-usable and suitable for further analysis. Second, by analyzing the phase and power of oscillations in V1, we provided new evidence supporting current hypotheses regarding high and low frequency oscillations in mice and the interplay between these waves through PAC. Further investigation, incorporating additional brain regions (such as higher-order visual areas), more complex task features (such as bias blocks), may lead to new insights and a deeper understanding of oscillations in predictive coding.

4.3 References

Aggarwal, Adeeti, Connor Brennan, Jennifer Luo, Helen Chung, Diego Contreras, Max B. Kelz, and Alex Proekt. 2022. "Visual Evoked Feedforward–feedback Traveling Waves Organize Neural Activity Across the Cortical Hierarchy in Mice." *Nature Communications* 13 (1): 4754. https://doi.org/10.1038/s41467-022-32378-x.

Benson, Brandon, Julius Benson, Daniel Birman, Niccolò Bonacchi, Matteo Carandini, Joana A Catarino, Gaelle A Chapuis, et al. 2023. "A Brain-Wide Map of Neural Activity During Complex Behaviour." *bioRxiv*, January, 2023.07.04.547681. https://doi.org/10.1101/2023.07.04.547681.

Bollimunta, Anil, Yonghong Chen, Charles E. Schroeder, and Mingzhou Ding. 2008. "Neuronal Mechanisms of Cortical Alpha Oscillations in Awake-Behaving Macaques." *The Journal of Neuroscience* 28 (40): 9976. https://doi.org/10.1523/JNEUROSCI.2699-08.2008.

Bonnefond, Mathilde, and Ole Jensen. 2015. "Gamma Activity Coupled to Alpha Phase as a Mechanism for Top-Down Controlled Gating." *PLOS ONE* 10 (6): e0128667. https://doi.org/10.1371/journal.pone.0128667.

Combrisson, Etienne, Timothy Nest, Andrea Brovelli, Robin A. A. Ince, Juan L. P. Soto, Aymeric Guillot, and Karim Jerbi. 2020. "Tensorpac: An Open-Source Python Toolbox for Tensor-Based Phase-Amplitude Coupling Measurement in Electrophysiological Brain Signals." *PLOS Computational Biology* 16 (10): e1008302. https://doi.org/10.1371/journal.pcbi.1008302.

Felleman, Daniel J, and David C Van Essen. 1991. "Distributed Hierarchical Processing in the Primate Cerebral Cortex." *Cerebral Cortex (New York, NY: 1991)* 1 (1): 1–47.

Gramfort, Alexandre, Martin Luessi, Eric Larson, Denis A. Engemann, Daniel Strohmeier, Christian Brodbeck, Roman Goj, et al. 2013. "MEG and EEG Data Analysis with MNE-Python." *Frontiers in Neuroscience* 7. https://www.frontiersin.org/journals/neuroscience/articles/10.3389/fnins.2013.00267.

Huang, Yanping, and Rajesh P. N. Rao. 2011. "Predictive Coding." *WIREs Cognitive Science* 2 (5): 580–93. https://doi.org/10.1002/wcs.142.

Huff, Trevor, Navid Mahabadi, and Prasanna Tadi. 2018. "Neuroanatomy, Visual Cortex."

IBL. 2024. "Unified International Brain Laboratory Environment." https://github.com/int-brain-lab/iblenv.

Jun, James J., Nicholas A. Steinmetz, Joshua H. Siegle, Daniel J. Denman, Marius Bauza, Brian Barbarits, Albert K. Lee, et al. 2017. "Fully Integrated Silicon Probes for High-Density Recording of Neural Activity." *Nature* 551 (7679): 232–36. https://doi.org/10.1038/nature24636.

Maris, Eric, and Robert Oostenveld. 2007. "Nonparametric Statistical Testing of EEG- and MEG-Data." *Journal of Neuroscience Methods* 164 (1): 177–90. https://doi.org/10.1016/j.jneumeth.2007.03.024.

Nestvogel, Dennis B., and David A. McCormick. 2022. "Visual thalamocortical mechanisms of waking state-dependent activity and alpha oscillations." *Neuron* 110 (1): 120–138.e4. https://doi.org/10.1016/j.neuron.2021.10.005.

Sassenhagen, Jona, and Dejan Draschkow. 2019. "Cluster-Based Permutation Tests of MEG/EEG Data Do Not Establish Significance of Effect Latency or Location." *Psychophysiology* 56 (6): e13335. https://doi.org/10.1111/psyp.13335.

Senzai, Yuta, Antonio Fernandez-Ruiz, and György Buzsáki. 2019. "Layer-Specific Physiological Features and Interlaminar Interactions in the Primary Visual Cortex of the Mouse." *Neuron* 101: 500–513.

Spaak, Eelke, Mathilde Bonnefond, Alexander Maier, David A. Leopold, and Ole Jensen. 2012. "Layer-Specific Entrainment of Gamma-Band Neural Activity by the Alpha Rhythm in Monkey

Visual Cortex." *Current Biology* 22 (24): 2313–18. https://doi.org/10.1016/j.cub.2012.10.020.

Tovar, David A., Jacob A. Westerberg, Michele A. Cox, Kacie Dougherty, Mark T. Wallace, André M. Bastos, and Alexander Maier. 2023. "Near-Field Potentials Index Local Neural Computations More Accurately Than Population Spiking." *bioRxiv*, January, 2023.05.11.540026. https://doi.org/10.1101/2023.05.11.540026.

Van Kerkoerle, Timo, Matthew W Self, Bruno Dagnino, Marie-Alice Gariel-Mathis, Jasper Poort, Chris Van Der Togt, and Pieter R Roelfsema. 2014. "Alpha and Gamma Oscillations Characterize Feedback and Feedforward Processing in Monkey Visual Cortex." *Proceedings of the National Academy of Sciences* 111 (40): 14332–41.

Vinck, Martin, Cem Uran, and Andrés Canales-Johnson. 2022. "The Neural Dynamics of Feedforward and Feedback Interactions in Predictive Processing." https://doi.org/10.31234/osf.io/n3afb.

Windolf, Charlie, Han Yu, Angelique C. Paulk, Domokos Meszéna, William Muñoz, Julien Boussard, Richard Hardstone, et al. 2023. "DREDge: Robust Motion Correction for High-Density Extracellular Recordings Across Species." *bioRxiv*, October, 2023.10.24.563768. https://doi.org/10.1101/2023.10.24.563768.